Improvements in Thomson Parabola studies: a new ImageJ script for spectral energy analysis and measurements using a double Image Plate detector

Contact javifer18@gmail.com, jalvarezruiz@gmail.com

Javier Fernandez Tobias

Central Laser Facility, Rutherford Appleton Laboratory
Science and Technology Facilities Council, Harwell Oxford
Didcot, Oxon, OX11 0QX

Jesus Alvarez Ruiz

Instituto de Fusion Nuclear, Universidad Politecnica de Madrid
C\Jose Gutierrez Abascal 2, C.P 28006 Madrid

Introduction

The Thomson Parabola diagnostic is a device that measures laser driven ions energy spectra and also identifies the particle species based on the charge to mass ratio. Basically it consists in both parallel and uniform electric and magnetic fields which deflect the ions from their initial propagation direction when accelerated by the laser. After traveling through the device, the particles are stopped on the Image Plate detector (IP) and create a signal which can be read out using a scanner in order to get the energy spectrum data. We report two new tools which help to interpret and extend the ion energy spectrum collected. On the one hand, we implemented an easy to run new ImageJ [1] script to calculate the energies from the recovered signal on the plates. On the other hand, we mounted a double IP detector which allows the measurement of high (>8 MeV) protons with better sensitivity.

Thomson Parabola dispersion relations

If we assume uniform electric and magnetic fields the dispersions in the vertical and horizontal directions perpendicular to the propagation of the incoming ions are given by

$$D_E = \frac{qEL_E}{mv_z^2}\left(d - \frac{1}{2}L_E\right)$$

$$D_B = \frac{qBL_B}{mv_z}\left(d - \frac{1}{2}L_B\right)$$

Where d is the distance between the beginning of the fields and the detector plane, v_z is the initial speed of the ions before entering the Thomson (which is used to calculate the energy) and L_E and L_B the distances over which the electric and magnetic fields extend [2] (fig.1).

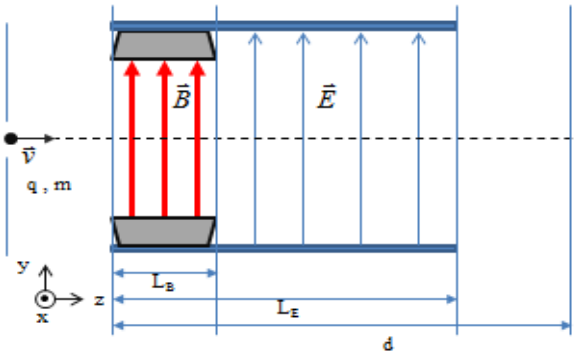

Fig. 1. Thomson Parabola diagnostic

The relationship between both dispersions can be easily obtained by the equations above

$$D_E = \frac{1}{q/m}\frac{EL_E}{(BL_B)^2}\frac{\left(d - \frac{1}{2}L_E\right)}{\left(d - \frac{1}{2}L_B\right)^2}D_B^2$$

As seen from this expression the signal trace has the shape of a parabola on the detector plane.

The ImageJ script*

The formula for the dispersion relations to retrieve the energy of the particles can be easily implemented on ImageJ creating a new script. Basically for given parameters of the electric and magnetic fields and the specifications of the Thomson geometry it calculates the ion speed before entering the device so the energy can be obtained straightforward. When running the code it asks for:

1. the image file to be analyzed (specifically the .inf file where the image dimensions are stored),
2. a tilting correction of the image if necessary,
3. the ion to be analyzed by entering its charge and mass,
4. the selection of four points of the parabola signal in order to get a fit of the dispersion relation parameters,
5. the radius of the Zero Point in pixels which will be used as the width of the region around the parabola to be inspected (fig. 2),
6. finally, background subtraction is carried out evaluating noise on the left and on the right of the signal region also with a width equal to the Zero Point radius.

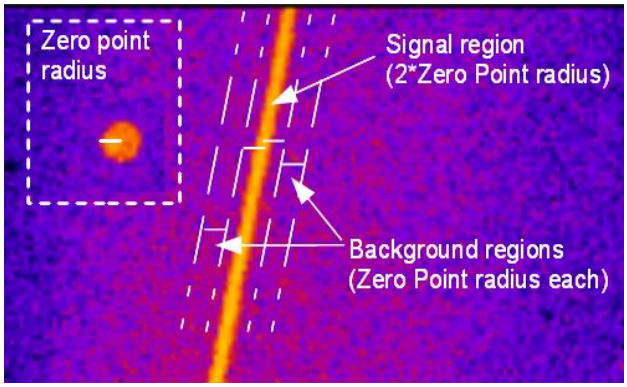

Fig .2. Proton signal collected by an Image Plate. The inset on the upper-left hand side represents the signal at the Zero Point. The radius is indicated by the while line. The main figure shows the three regions used by the script to calculate the intensity of the signal and the background.

In return, it will calculate the intensity of each pixel in Photo Stimulated Luminescence (PSL) values and finally it will give the spectrum by obtaining the energies of those pixels via the dispersion relations given before. The final intensity will be the sum of the PSL values of the pixels in every energy bin. So for example, if we choose 300 bins and an energy step of 0.1 MeV, the energy window will extend from 0 to 30 MeV, and the intensity in each bin will be the sum of the intensities of the pixels stored in the considered bin converted into PSL.

Results

It is important to remark that the script works with given values of the Thomson specifications such as its length and distances over which the fields extend and the values of the electric and magnetic fields. For a different Thomson parabola one needs to modify these values in the script to get the suitable calculations. In the following figure we show the results obtained with the script for a proton beam generated from a 10µm CD (deuterated plastic) target for a Thomsom Parabola with values of B=0.985T for the magnetic field (one field is sufficient to get the energy so the E-field value is not needed), l=50mm for the magnet length and d=361mm from end of magnet to detector. (fig. 3a). During the execution the script will display dialog boxes showing the the parabola fit (fig.3b) and the spectrum (fig. 3c). Besides, it will automatically save the spectrum data (signal PSL, background PSL and the input parameters in a .txt file.

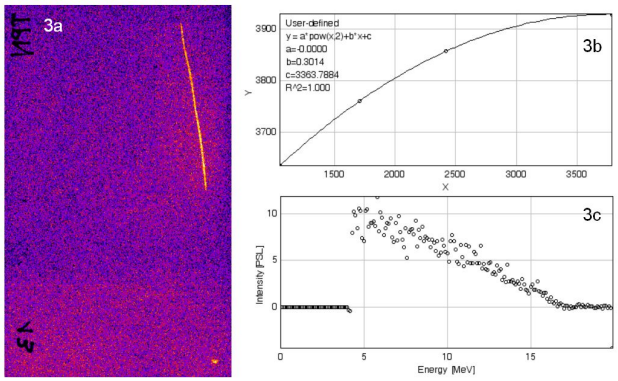

Fig.3. a) Ion signal on the IP; b) parabola fit dialog box; c) spectrum dialog box.

Double Image Plates to account for high energy protons

Protons with high kinetic energy can get through the IP giving barely any signal so that in order to increase the energy detection threshold of the detector we placed two plates one after the other. If we know the materials of the layers that form the IP and their thicknesses we can check using SRIM [3] the minimum input energy for the protons to get through the first plate and reach the back one, and compare this value with the one given by the code. The plates used were model BAS-TR, which consist in a 50µm thick phosphor layer, a 250µm one made of plastic (we will use polystyrene to model this using SRIM) and a magnet of 160µm thick made of Ferrite [4]. The following graph shows the energy distribution calculated using the ImageJ script when the irradiated target was 160nm Al coated + 3000um BorSiO2 and the laser energy delivered 565,2J. The blue points correspond to the spectrum collected on the front Image Plate and the red points correspond to the spectrum at the back (fig.4).

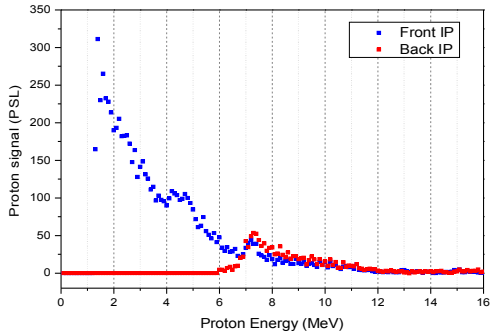

Fig. 4. Proton spectrum on front and back IP calculated using ImageJ script.

As it can be seen from the graph, the proton signal seems to appear on the back Image Plate above 7 MeV reaching its maximum at 7.5 MeV and decreasing for higher values.

The SRIM simulation is performed next where the input parameters are the energy, the layers of the different materials of the IP and their thicknesses. The SRIM simulation shows that protons of 7.5 MeV can already get through the front IP (fig. 5). There is a mismatch of around 0.5 MeV which can be attributed either to deviations of experimental parameters (such as effective magnetic field or geometric distances) or to the materials and densities employed to simulate the IPs in SRIM.

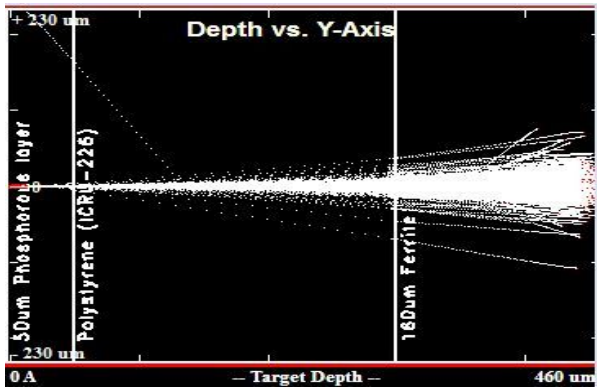

Fig. 5 SRIM simulation for protons going through the 460um Image Plate for an input energy of 7.5 MeV. The protons have enough energy to exit the final end of the Ferrite layer.

One feature worth mentioning when using a double IP is the fact that the the spectrum which corresponds to the signal on the front plate often presents a bump at the same proton energy at which the signal on the back plate starts to appear (see fig.4 around 7.5 MeV). To our knowledge, there is no reason for this revival of the signal since the blue curve should be continuously decreasing to zero. Is this effect due to the recoil of the protons from the back plate? Further studies need to be carried out using two plates to explain this unexpected feature.

Making use of SRIM and the conversion factor between deposited energy and generated PSL values (for this kind of plates, it is known that 1 MeV of deposited energy in the active layer of the IP roughly produces 0,185 PSL [5]), we calculated the calibration tables for both IP in order to retrieve total number of protons (to a good approximation this procedure can be applied to light ions). Figure 6 shows the resulting conversion from the PLS values in fig.4 to number of protons.

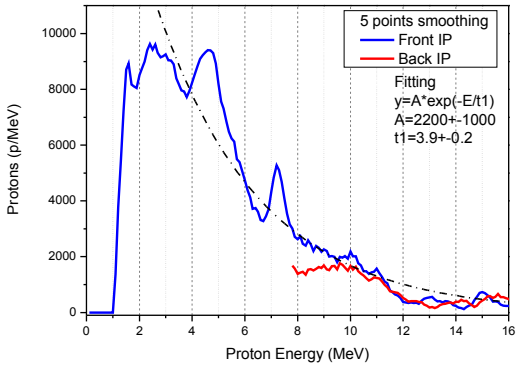

Fig. 6 Calibrated proton spectrum on front and back IP and fitted distribution.

At a first sight one can see that the first IP already contains the same information for high energy protons than the second IP, thus indicating that there might be no reason to use a Double IP detector. However, as it is shown in figure 7, the response of the

second IP plate improves the detection efficiency up to a factor of three for energies between 7.5 and 12 MeV. Thus, for experiments aiming at the production of high energy ion, it would be convenient to use the Double IP arrangement.

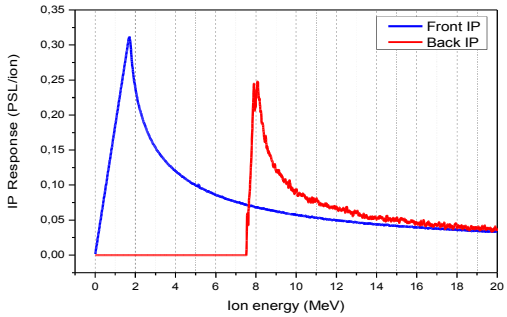

Fig. 7. PLS induced on the active layers in the front (blue) and rear (red) Ips for different proton energies.

Future work

At present, the PSL spectrum obtained with the created ImageJ script does not take into account the effect of the fading (decay of signal in the active layer of the IP with time) due to the time delay between the irradiation of the IP and the retrieval of the signal with the scanning. This option is planned to be included in the script in the near future.

As for the absolute calibration of the IPs, it is the aim of the authors to perform an experimental campaign at an Ion acceleration facility to obtain the "energy deposited to PSL" conversion factor for different models of Image Plates, ion species and energy ranges to extend and complement those already done for protons and deuterons over the range 0.6-3.4 MeV [5] and from 0.9-5.4 MeV alpha particles [6].

Conclusions

A new ImageJ script has been developed for calculating the Thomson parabola ion spectrum. It is an easy-to-run pluging that gives a very quick view of the ion spectrum which can be useful when working in the lab to get an idea of how the spectrum looks like. Since it is integrated in ImageJ it has the advantage of allowing the use of other functions in ImageJ such as zooming, flipping and rotating images, operation between images and adjusting the contrast while running the code. It also converts the pixel intensity to PSL values and gives a parabola fit for the signal. Using this script a study of the use of two IP's has been done to extend the range of proton detection. Calculations show that the double IP detector improves the detection efficiency up to a factor of three for energies between 7.5 and 12 MeV. As a trade off, artificial signals can be created in the first IP for those energy values.

Acknowledgements

Proton data for this study comes from D. Carroll experimental campaign *measurement of magnetic fields generated by hot electrons within glass targets* in VULCAN TAP on October 2012. We would like to thank the members of the experimental group of Strathclyde University of Glasgow and the Queen's University of Belfast group, especially Domenico Doria. We also want to thank Dr. D. Neely for suggesting the implementation of the Double IP detector and his useful comments when elaborating this work.

References

1. W.S. Rasband, ImageJ, U. S. National Institutes of Health, Bethesda, Maryland, USA, http://imagej.nih.gov/ij/, 1997-2012.
2. D.C. Carroll et al. Nuclear Instruments and Methods in Physics Research A 620 (2010) 23–27
3. J. F. Ziegler, J.F. , M.D. Ziegler, J.P. Biersack. Nuclear Instruments and Methods in Physics Research, B 268 (2010) 1818
4. H. Ohuchi, A. Yamadera. Nuclear Instruments and Methods in Physics Research A 490 (2002) 573–582
5. A. Mančić, J. Fuchs, P. Antici, S. A. Gaillard, and P. Audebert Review of scientific instruments 79, 073301 (2008)
6. C. G. Freeman, G. Fiksel, C. Stoeckl, N. Sinenian, M. J. Canfield, G. B. Graeper, T. Lombardo, C. R. Stillman, S. J. Padalino, C. Mileham, T. C. Sangster, and J. A. Frenje Review of scientific instruments 82, 073301 (2011)

*Link to download the ImageJ script: https://github.com/Jalvarezruiz/Thomson_Parabola (Licence GPL)

Use of Bubble detector spectrometer for neutron sources driven by high power lasers

Contact *jgreen11@qub.ac.uk*

A. Green, S. Kar

Department of Physics and Astronomy,
Queen's University Belfast
Belfast BT7 1NN

H. Powell

Department of Physics, SUPA
University of Strathclyde
John Anderson Building
107 Rottenrow
Glasgow G4 0NG

Introduction

The rapid advances in laser technology in the past two decades have enable the use of laser accelerated ions to generate laser-driven fast neutron sources which provide a cheaper and more compact alternative to spallation and fission based sources.[1]

Among the many advantages such a neutron source would bring are applications in materials testing for future fusion reactors, scanning large amounts of cargo for contraband, and potential use in transmuting nuclear waste.[2][3]

In an experimental campaign that took place during August and September 2012, deuterons were accelerated using the Petawatt laser facility at Vulcan from thin (~10μm) deuterated plastic targets into thicker (~several mm) targets of the different materials. The resulting D-D beam-ion fusion reaction produced neutrons of high flux and energy centred around 2.45 MeV.

Typical neutron time-of-flight (n-ToF) diagnostics in such experiments consist of plastic scintillators light-coupled to PMTs. These can be very sensitive to the strong x-rays produced via Bremsstrahlung when the laser interacts with the solid target. As such, a Bubble Detector Spectrometer (BDS) was used to spectrally resolve the neutron flux produced in the experiment, and calibrate the n-ToF diagnostics, as it is insensitive to x-rays.[4] The bubbles are easily counted by eye, as can be seen in the Fig.1.

Fig.1 A single bubble detector tube with visible bubbles

Operating principle of the Bubble Detector Spectrometer

The clear polymer that makes up the detectors has tiny droplets of liquid dispersed through it. When a neutron passes through this droplet, the droplet vaporizes and a visible gas bubble is seen in the detector. Information about the exact chemical composition of the clear polymer and dispersed liquid are protected by patent and not released by the manufacturers. (Bubble Technology Industries, Canada)[4] In addition to the spectrometer discussed here, there is also a spectrally integrated dosimeter detector available. The BDS can be easily reused after being recompressed using a recompression chamber supplied by the manufacturers.

The BDS consists of six sets of detectors, with all of the detectors in a set being sensitive to a given range of neutron energies. The 6 energy bins of the detectors are shown in the table below.

Name	BDS-10	BDS-100	BDS-600	BDS-1000	BDS-2500	BDS-10000
Energy Range(MeV)	0.01-0.1	0.1-0.6	0.6-1.0	1.0-2.5	2.5-10	10-20

Table 1. Energy bins of bubble detectors

The normalized response of different detectors corresponding to different energy bins can be seen in figure 2, and can be used to relate the number of bubbles seen in the detectors to neutron flux via the equation

$$\overline{\boldsymbol{R_i}} = \boldsymbol{\sigma_{ij}} \cdot \boldsymbol{N_j} \quad (1)$$

Where $\boldsymbol{\sigma_{ij}}$ is the averaged cross section of a reaction by the detector with incident neutrons (as shown in fig 2.), *i* is an index for the different detectors, and *j* is an index for the different region of the histogram seen by the detector. The total flux of neutrons (in n/cm^2) seen by the detector in this threshold is denoted by $\boldsymbol{N_j}$ and can be calculated easily once the average number of bubbles, $\overline{\boldsymbol{R_i}}$, across all detectors of that energy range is known.

Since the detectors corresponding to different energy bins are sensitive to discrete band of neutron energies, the energy resolved neutron flux is obtained by a simple deconvolution of the neutron fluxes seen by different detectors.

The stripping process starts with the BDS-10000 detectors, which can detect only the highest energy bin of the histogram.

$$\overline{\boldsymbol{R_6}} = \boldsymbol{\sigma_{66}} \cdot \boldsymbol{N_6} \quad (2)$$

where $\boldsymbol{\sigma_{66}}$ is the average response of the BD-10000 detector over the interval 10 – 20 MeV. Having determined this, it is possible to solve for the next energy bin by solving the equation

$$\overline{\boldsymbol{R_5}} = \boldsymbol{\sigma_{55}} \cdot \boldsymbol{N_5} + \boldsymbol{\sigma_{56}} \cdot \boldsymbol{N_6} \quad (3)$$

Here, $\boldsymbol{\sigma_{56}}$ is the sensitivity of the BD-2500 detector over the 10 – 20 MeV range, and $\boldsymbol{\sigma_{55}}$ the sensitivity of the same detector over the 2.5 – 10 MeV range. $\boldsymbol{N_6}$ is known from equation (2) and $\overline{\boldsymbol{R_5}}$ is measured from the BDS-2500 detectors.[4] This process of deconvolution is carried out through each of the 6

areas of the histogram in order to obtain the neutron flux at the six different energy bins.

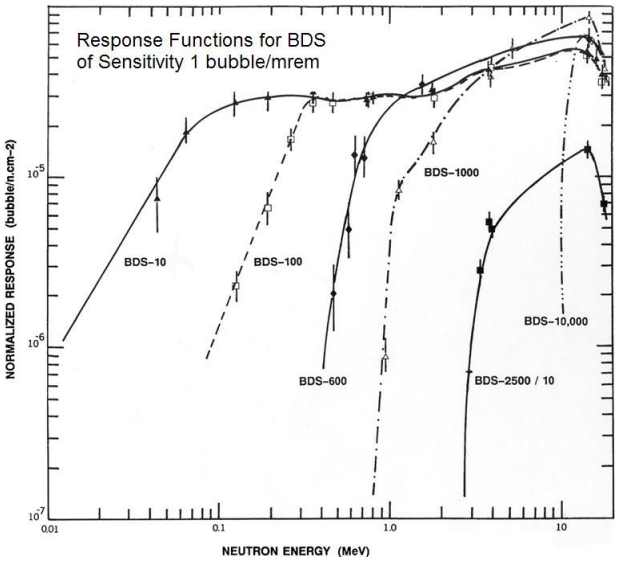

Fig.2 Response functions for bubble detectors as a function of neutron energy.[4]

An error for the deconvolved neutron fluxes can be calculated using the uncertainties in the counts from each group of detectors. The uncertainties in each bin of the spectrum arise because there are statistical uncertainties in the measured counts from the detectors. The counts in the detectors have an uncertainty equal to the square root of the number of counts observed in the detector. Each bin in the deconvolved neutron spectrum may have contributions to its uncertainty that arise from uncertainties from all of the individual bubble counts. After the deconvolution process described above, the number of bubbles counted for a single detector sensitivity are artificially incremented by one standard deviation, and then the deconvolution process is repeated to make an artificial spectrum (i.e. for one value of *i* set $\overline{R_i}$ equal to $\overline{R_i} + \overline{\delta R_i}$ and repeat the deconvolution)[4]

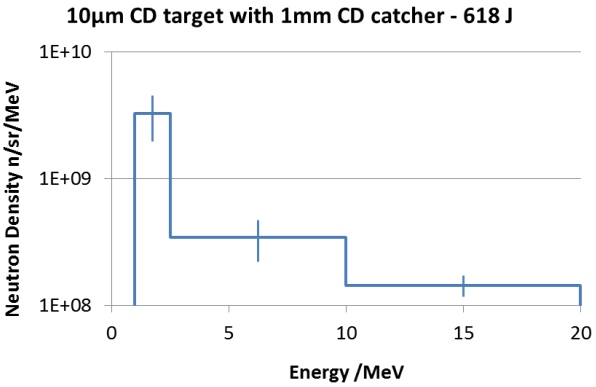

Fig 3. Histogram of Neutron Density for a typical pitcher-catcher target arrangement

The difference between these two unfolded spectra is calculated. For each bin this yields the uncertainty in the spectrum due to the count from one bubble detector. This can be repeated for all detector sensitivities.

Because the counts are statistically independent, so are the calculated differences in each energy bin. Since they are independent, the total contribution to each bin is the sum-in-quadrature of the differences. Thus the error on each energy bin is found.

Experimental Method

In this experiment, the petawatt beam of the Vulcan laser was used to deliver 200J of energy onto the target in 700fs and a focal spot of the order of 5µm via an f/3 off-axis parabola and plasma mirror set-up.

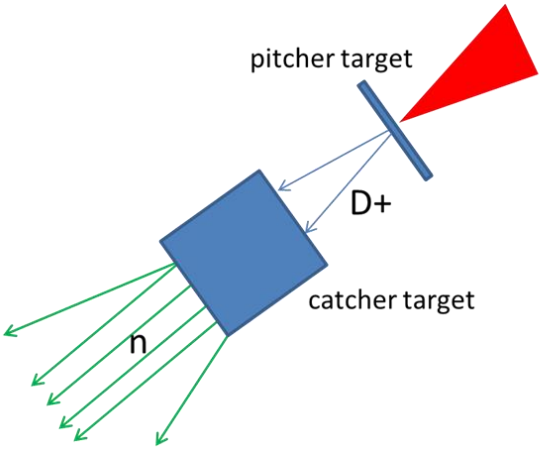

Fig. 4 Typical pitcher-catcher target set-up used in this experiment.

In order to obtain significant number of bubbles in the detectors, which is required for a good statistics, the detectors were held at atmospheric pressure inside a small pressure vessel which could be placed inside the interaction chamber close to the neutron source. In the experiment discussed in this report, the BDS was placed at a distance of 75cm from the source of neutrons. Shielding of the detectors from ions, electrons and gamma rays was not required as they are insensitive to these forms of radiation. For experimental conditions where lower neutron flux is expected, one can accumulate the bubble formation over a number of identical shots in order to obtain reliable statistics.

Results and analysis

After the laser shot on the target, the bubble detectors were removed from the interaction chamber and the number of bubbles in each of the detectors was counted manually. The analysis for obtaining the neutron spectrum from the number of bubbles was done by using a spread sheet provided by the manufacturers, which calculates by the deconvolution procedure explained above, the histogram of neutron flux in the six different energy bins.

Fig. 3 shows a typical neutron spectrum obtained in the experiment. In this case the neutrons are produced by the D-D fusion reaction in a pitcher-catcher configuration.
As can be seen from the spectrum, the highest neutron flux was seen in the 1.0 – 2.5 MeV energy bin, which corresponds to the characteristic neutron energy from the D-D reaction. The flux of neutrons seen in this shot is in good agreement with the data obtained from the nuclear activation diagnostics deployed simultaneously in the same shot.

The energy of the neutrons produced from the fusion reaction in the laboratory frame (E_3) can be expressed in terms of a kinematic equation of the kinetic energy released by the

reaction (Q) , the mass of the particles involved (stationary and energetic deuterium nuclei (m_1, m_2), emitted neutron (m_3) and He^3 ion (m_4)), the energy of the incident deuteron (E_1) and angle of emission of neutrons with respect to the angle of incidence of the deuterons (θ).[5]

$$E_3 = \left[\frac{m_1 m_3}{(m_3+m_4)^2} + \frac{m_2 m_4}{(m_1+m_2)(m_3+m_4)}\right] E_1 + \frac{m_4}{m_4+m_3} Q + 2\left[\frac{m_1 m_2 m_3 m_4}{(m_1+m_2)(m_3+m_4)^3} \times \left({E_1}^2 + \frac{m_1+m_2}{m_2} Q E_1\right)\right]^{1/2} \times \cos\theta \quad (4)$$

The second term of the equation gives a neutron energy of 2.45 MeV. The first term gives rise to an increasing energy of emitted neutrons with increasing incident deuteron energy, and the third term gives a variation with angle. The higher energy neutrons (10-20 MeV) seen in the neutron spectra shown in the fig. 3 histogram can be explained via this first term for an ion energy of the order of 10 MeV, which was typically produced by the Petawatt laser interaction with the pitcher target.

Conclusion

The Bubble Detection Spectrometer is an absolutely calibrated diagnostic for measuring neutron flux at different range of neutron energies, from epithermal to fast neutrons. It can be used in the experiment primarily as a tool for diagnosing a neutron flux and calibration other diagnostics, and as a complement to these diagnostics.

Being insensitive to X-rays, gamma rays etc., the BDS brings substantial flexibility in terms of obtaining reliable measurements in harsh environments such as the high power laser-plasma interaction. There is no risk of damage to the detectors themselves, and they can be freely placed to measure the neutron spectrum at different positions. The analysis is very straightforward and provides absolute values of neutrons.

The main limitation of the spectrometer however is the width of the energy bins, with it being unable to resolve a high resolution neutron spectrum. With a maximum detectable energy of 20 MeV, and future experiments hoping to achieve neutron energies in excess of this (by means of different nuclear reactions or by high-energy beam-fusion reactions), suitable moderation must be employed between the neutron source and bubble detectors. Especially since an error in reading any singular set of detectors will introduce errors in all other energy bins.

References

[1] T. Ditmire, J. Zweiback, V. P. Yanovsky, T. E. Cowan, G. Hays & K. B. Wharton *Nature* **398** 489 **(1999)**

[2] L.J. Perkins, B.G. Logan, M.D. Rosen et al. *Nuclear Fusion* **1** 40 (2000)

[3] A. Buffler, *Radiat. Phys. Chem*. **71**, 853 (2004)

[4] BTI Bubble Detector Spectrometer BDS Manual (2012)

[5] N. Izumi et. al. *Phys. Rev. E.* **65** 036413 (2002)

Temporally and spatially resolved measurements of fast electron dynamics using a chirped optical probe

J. S. Green, N. Booth, D. Rusby, L. Wilson
Central Laser Facility, STFC
Rutherford Appleton Laboratory, Chilton, Oxon, OX11 0QX

C. D. Murphy
University of Edinburgh
Mayfield Road, Edinburgh, EH9 3JZ

R. J. Gray, D. A. MacLellan, P. McKenna
University of Strathclyde
107 Rottenrow, Glasgow, G4 0NG

R. J. Dance
York Plasma Institute, University of York
Heslington, York, YO10 5DD

Introduction

The study of fast electron transport in solid targets is crucial for many key applications, yet the ability to diagnose various transport processes within the target remains an issue. A number of experiments have worked to address the challenge of diagnosing fast electron beam temperature, number density and beam divergence. Of these, both diagnosing and controlling the fast electron beam divergence is perhaps the greatest challenge.

Early on, transverse optical probing of the target rear surface was used to infer a fast electron distribution at the rear of the target [1], with OTR used to measure the highest energy electrons as they leave the target rear surface [2]. Complementary measurements of optical probing combined with Cu K-alpha and XUV imaging [3] inferred a large fast electron divergence angle (> 50°) in a ballistic transport regime, with Green et al. [4] observing that the fast electron divergence angle increases with laser intensity when a broad range of diagnostic techniques are considered.

Studies of Target Normal Sheath Acceleration (TNSA) of protons and ions, namely measurements of the rear surface ion source size, have also been used to diagnose fast electron distribution and subsequent sheath field evolution [5,6]. However as the target thickness reduces to the order of the pulse length ($d < c\tau$) the rapid transverse expansion (close to c) of the accelerating sheath fields [6,7], typically attributed to electron recirculation, can lead to an ion source size much larger than that which might be expected from even the most divergent fast electron beam.

Temporally resolving the formation of these intense sheath fields could not only help to diagnose the early-time fast electron distribution, but when used in conjunction with ion source size measurements, could shed light on the timescales of ion acceleration, for which not a lot is currently known for short pulse (< 100 fs) laser systems.

Diagnostic outline

The characteristic formation of a plasma at the target rear surface during TNSA, on the order of the Debye length, is a direct result of field-induced barrier suppression (FIBS) ionisation that occurs rapidly under the influence of intense TV/m electric fields.

Optical light incident on the rear surface prior to the high-intensity interaction would reflect off a cold solid, as governed by Fresnel's law. With the formation of a localised plasma at the rear surface, optical light propagates into a steep plasma gradient, before being reflected at the critical plasma density. The probe polarisation and plasma density profile are key factors in understanding any localized changes in reflectivity but the required analysis and modeling are beyond the scope of this report.

Careful measurements of the modified reflectivity profile on the target rear surface can be used to temporally-resolve sheath formation, permitting crucial measurements of the initial, and late time, fast electron distribution to be made.

For many experiments it is preferable to probe at multiple time steps on a single shot rather than perform a delay scan over many shots. In order to achieve this the optical probe can be temporally chirped and the collected light imaged onto an optical spectrometer. This method gives a direct relation between optical frequency and time. Although it should be noted that the time resolution of the system Δt is typically limited not by the spectral resolution of the spectrometer but by the relation [8]:

$$\Delta t = \sqrt{\tau_0 \times \tau_c}$$

where τ_0 and τ_c are the bandwidth-limited and chirped pulse durations respectively.

An early example of this technique was reported by Benuzzi et al. [9] who studied the change in optical reflectivity on plain Al targets when subject to X-ray pre-heating and laser-driven shocks generated by a modest laser intensity of 6×10^{13} Wcm^{-2}. Pre-heating of the rear surface to just 0.4 eV was seen to lead to a marked drop in reflectivity from 90% to 60% over ~100 ps.

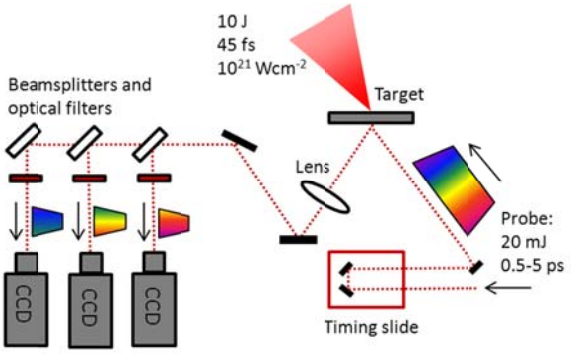

Figure 1 – Astra-Gemini diagnostic layout showing the chirped optical probe reflecting off the target rear surface before being imaged onto three CCD cameras, each filtered to view a specific wavelength range and hence temporal snapshot.

Antici et al. [10] extended the technique to look at hot electron dynamics for higher intensity interactions (5×10^{19} Wcm^{-2}). The authors probed the target rear surface with ~4 ps resolution, making 1D spatial measurements of the probe's phase in order to extract data on the shape of the plasma expansion and fast electron distribution.

Here we present a new implementation of rear surface optical probing that for the first time yields multiple, temporally-resolved, 2D images from a single shot by using a novel

spectral filtering method. With temporal resolution as short as 100 fs, and spatial resolution of ~5 µm, electron dynamics at ultra-high intensities can be probed for a range of targets and laser parameters.

Experimental set-up

The experiment was carried out on the Astra Gemini laser at the Central Laser Facility. Astra Gemini is a dual-beam Ti:Sapphire 800 nm laser that delivers 10 J of energy on target per beam with a pulse duration of 45 fs. One of these beams was focused on to target at 30 degrees incidence using an f /2 parabola resulting in a Full Width Half Maximum (FWHM) spot size of 2.5 µm. Approximately 30% of the incident laser energy was contained within the central focal spot, resulting in a peak intensity of ~10^{21} Wcm^{-2}.

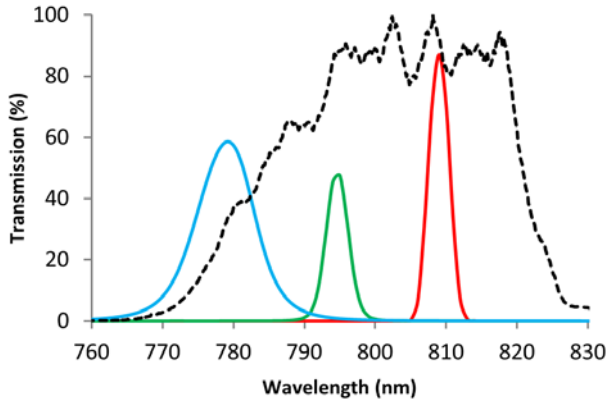

Figure 2 – Optical filters (coloured lines) used to isolate narrow portions of the Astra Gemini spectrum (dashed line). Using the linear chirp of the beam, each filter effectively selects a narrow time window for observation.

For the rear surface optical probe the other arm of Astra Gemini was chirped from 45 fs to 0.3 – 5 ps by detuning the compressor. The p-polarised beam was then apodised down to 10 mm and directed on to the target rear surface at an angle of 40 degrees (relative to target normal). The probe beam contained approximately 20 mJ of energy, with a maximum intensity on target of 5x10^{10} Wcm^{-2}.

The timing of the optical probe relative to the main interaction was varied with the use of a remote timing slide in the Astra Gemini laser area. The t=0 point was established by focusing the main pulse in air at low intensity and altering the relative timing of the probe beam until the initial plasma formation was just visible.

The reflected probe light was collected using a f/6 achromatic lens, achieving a magnification of x6.7 and a spatial resolution of ~5 µm. In order to achieve temporal separation the imaged probe beam was split between three CCD cameras, each having a different narrow-pass filter in place to isolate one section of the linear chirp. By using this technique, rather than an optical spectrometer, we were able to obtain three different snapshots in time combined with 2D spatial information. The filters chosen to isolate each channel are shown in Figure 2.

Initial results

A number of Al and CH target foils were irradiated during the course of the experiment, with thicknesses varying from 100 nm to 150 µm. Each target foil was mounted in a 5x5 array, with a 1 mm clear circular aperture for each target position. Figure 3 shows three images of a 50 µm Al foil captured on a single shot at +5, +6.5 and +8 ps. The images have been normalised with respect to the pre-shot reference image in order to show a 2D reflectivity profile at each time step.

Figure 3 shows a large (~250 µm diameter) region of lower reflectivity that expands radially outwards, with the average reflectivity dropping from 42% to 31% within the bounds of the feature over 3 ps. It is interesting to note that there is a noticeable degree of horizontal asymmetry. This is most likely attributed to the angle of the target with respect to the optical probe. Probe light incident on the right edge of the target foil would arrive approximately 2 ps before that illuminating the left hand edge, hence you would expect to see an earlier profile of the sheath evolution as you look from left to right. Indeed this temporal gradient can be used to extract extra data if carefully deconvolved.

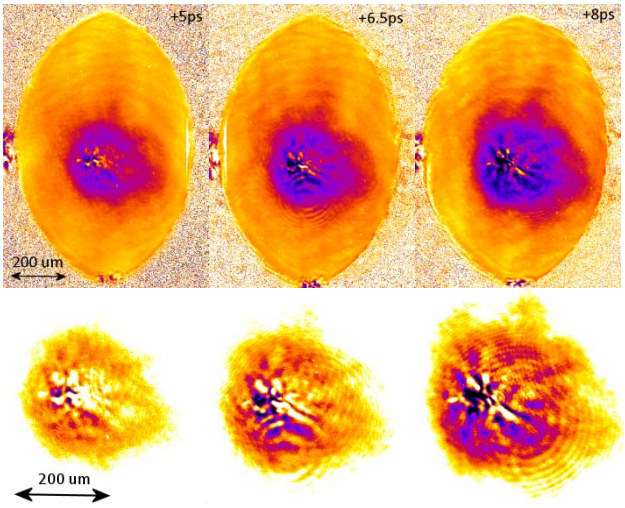

Figure 3 – Rear surface reflectivity profile for a 50 µm Al foil 5-8 ps after the main interaction. Lower image shows central detail. Note: viewing angle of the target means that the horizontal dimension is contracted.

In the central region of lower reflectivity, several filamentary-type structures can be seen with features on a scale of ~10 µm. Within these structures reflectivity falls to below 10%, suggesting that the probe light is either being strongly absorbed or refracted / scattered out of the cone angle of the collection optic.

Conclusions and Future Development

A novel method of temporally and spatially resolving sheath formation on the rear surface of targets has been implemented. With spatial resolution of 5 µm and variable temporal resolution of 100 fs – 1.5 ps, the diagnostic is capable of resolving rapid changes in target reflectivity which can be used to infer valuable information on fast electron transport and plasma formation.

From a single shot on the Astra-Gemini laser a rapidly expanding region of low reflectivity 5-8 ps after the interaction can be seen on the target rear surface, and fine structured filamentary features resolved. Future developments will see the addition of an interferometry line in order to characterize the plasma density scale lengths alongside existing reflectivity measurements.

Acknowledgements

The authors would like to thank the staff at the CLF for all of their valuable assistance during the experimental campaign.

References

1. Tatarakis M. et al. *Phys. Rev. Lett.* **81** p999 (1998)
2. Santos J.J. et al. *Phys. Rev. Lett.* **89**, 025001 (2002)
3. Lancaster K.L. et al. *Phys. Rev. Lett.* **98**, 125002 (2007)
4. Green J.S. et al. *Phys. Rev. Lett.* **100**, 015003 (2008)
5. Cowan T.E. et al. *Phys. Rev. Lett.* **92**, 204801 (2004)
6. McKenna P. et al. *Phys. Rev. Lett.* **98**, 145001 (2007)
7. Quinn K. et al. *Phys. Rev. Lett.* **102**, 194801 (2009)
8. Geindre J.-P. et al. *Opt. Lett.* **26**, 1612 (2001)
9. Benuzzi A. et al. *Phys. Plasmas* **5**, 2410 (1998)
10. Antici P. et al. *Phys. Rev. Lett.* **101**, 105004 (2008)

Investigations into Generation of Neutron Spectra from High Powered Laser Sources via the Use of Activation Foils

Contact *rob.clarke@stfc.ac.uk*

S. Dorkings, R. Clarke
CLF, STFC Rutherford Appleton Lab
Oxfordshire, OX11 0QX

S. Kar
Dpeartment of Physics and Astronomy, Queen's University Belfast
Belfast BT7 1NN

Introduction

Neutron activation can be used as a useful diagnostic tool for determining the energies and quantity of neutrons produced during an interaction. In this experiment, neutrons were produced by inducing D-D fusion by accelerating Deuterium ions within deuterated plastic foils using the Petawatt laser system at the Vulcan laser facility. This experiment took place during August and September 2012.

The aim of this investigation was to attempt to use activation materials to build energy spectra of neutrons created by a laser source. A study at JET[1] found that the use of activation 'packs' could be used to measure the flux of neutrons at various locations within their chamber. Similar processes will be used, but with the single purpose of determining neutron energies created by the laser interaction.
This could be used as an interesting accompaniment to current neutron diagnostics, or as a simple standalone diagnostic.

One major advantage of activation foils is that they can discriminate between particle types and can also be safely placed close to the hostile laser interaction. This could allow for a more accurate observation of the neutron flux created from the laser source.

Theory

The neutrons produced by the laser interaction can be used to generate nuclear reactions within the target foils. The reactions that are expected to be observed are (n,p), (n,γ) and the (n,2n) reaction produced by incident neutrons with higher energies. After the parent nuclide has undergone one of these reactions, the resulting nuclide is likely to be unstable and decay. These decays generally produce characteristic gamma photons with varying efficiency depending on the mode of decay. These photons and used to determine the identity as well as quantity of nuclides produced within the sample.

The energy cross section of a reaction may be used to deduce the energy range of incident neutrons. By taking an average value of this cross section across the energy range, an estimate of the number of neutrons present can also be made.

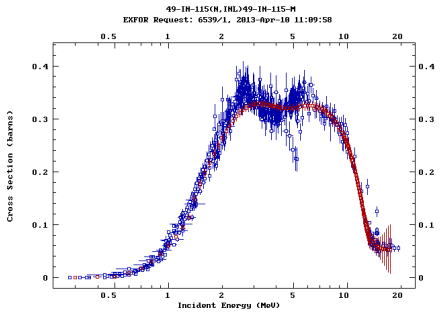

Fig 1. Cross section of the ^{115}In (n,n) ^{115m}In neutron scattering reaction[2].

The probability of any incident neutron causing a reaction within the target material is given by the equation:

$$\frac{N_0}{n_i} = P = \frac{N(AT)\sigma}{A} \qquad \textbf{(1)}^{[3]}$$

Where N_0 is the number of nuclei produced, n_i is the number of incident neutrons, P is the probability of a reaction, N is number of nuclei per unit volume, A is area of bombarded material, T is the thickness of material, and σ is the cross section of the reaction.

The initial number of nuclides created, N_0 of a given product may be found by using the modified decay equation to find the number of nuclides at the time of the shot.

$$n_r = \frac{\Delta n}{e^{-t_i} - e^{-t_f}} \qquad \textbf{(2)}$$

Δn is the total number of decays that have occurred during the scan, t_i is the start time of the scan relative to the time of the initial activation, and t_f is the end time of the scan relative to the initial activation.

Once N_0 has been calculated, the incident number of neutrons n_i can then be calculated using equation (1). If different nuclides are produced within the sample foils with varying energy cross sections a spectrum of neutrons may be built by comparing each.

Experimental Method

The activation foil materials utilised during this investigation were: iron, zinc, indium and tantalum. These were present as 50x50mm x1mm foils. There were two samples of Indium and Tantalum available, and were alternated between neutron exposures to allow for activated products to decay to negligible levels. The zinc and iron samples were replaced with new foils for every interaction due to long half life products created in significant quantity.
The foils were initially arranged in a 100x100mm grid 100mm from target along the laser axis to expose the foils to the highest neutron flux. Towards the end of the investigation, the distance of the samples to the target was reduced to 58mm in order to increase the activation signal.

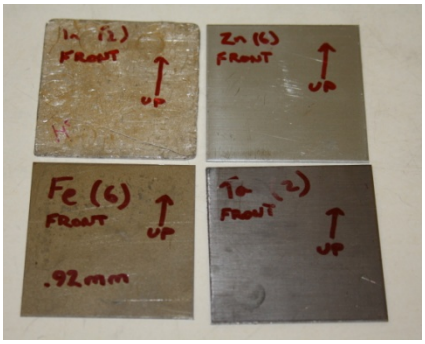

Fig 2: Image of some activation foils used, in the same configuration as presented to the laser target.

To prevent the activation of Indium by thermal neutrons, the surface of the samples facing the target were shielded by 1.5mm PTFE. This will also absorb any heavy ions created during the interaction and other target debris. As the experiment progressed, a second layer of PTFE was added to shield the rear surface of the targets to prevent any backscattered neutrons from interacting with the foils.

Once the foils have been exposed to neutrons generated from the laser pulse, the interaction chamber was let up from vacuum and the foils removed and transferred to the radiation lab. Here they are placed on an absolutely calibrated Canberra High Purity Germanium (HPGe) detector (Model: GR2518) shielded with low activity lead. The samples were left on the detector for differing integration times to build up gamma spectra, in order to best observe emissions from both long and short half lives. The spectra were compiled and analysed using Canberra's Genie 2000 software.

Peaks observed in the gamma spectra were compared with potential sources listed in the Berkley Laboratory Isotopes Project[4] database. Potential isotopes for each line were found using the search tool through a combination of half lives, and atomic mass/ number. The half lives of the products were compared using data taken over several scan durations.

Once activation products and their corresponding nuclear reaction are identified, the number of nuclei of each isotope may be calculated. The integrated emission of each peak was determined from the spectra compiled by the Genie software, and adjusted for the efficiency of the detector and detector geometry where applicable. The resulting figure is used with equation (2) to determine the initial number of nuclei of each activated nuclide species. Equation (1) is then used to calculate the number of neutrons incident on the foils.
The energy dependant cross sections for each reaction enable an energy spectrum of the neutrons generated from the laser- target interaction to be deconvoluted.

Results and Analysis

A total of 11 separate laser interactions with a variety of laser target configurations were measured. In each case, all of the activation foil materials were present, and the samples removed from the interaction chamber as soon as possible. The activation foils were then transferred to the HPGe to initiate scans of the gamma spectrum between ~40keV and 2000keV. Although the detector still responds to photons of higher energy than 2000keV, the low efficiency meant that no emissions were detected with any reliability from activated nuclides.

The gamma spectra observed were analysed and products identified from the characteristic energy peaks associated with the isotope decays.

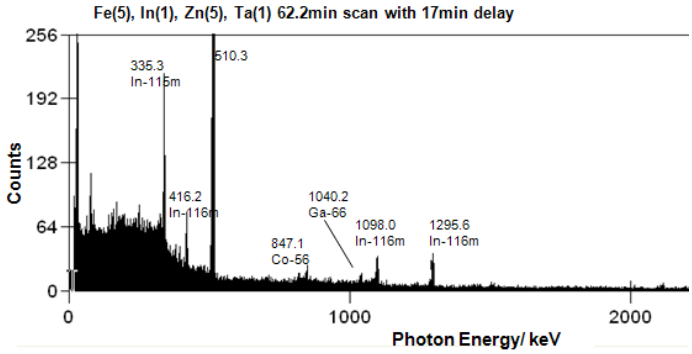

Fig. 3: An example of a HPGe scan using all sample foils after becoming activated during laser interaction. Here the energy peaks in the gamma spectra have been labelled along with the nuclides responsible for these emissions. This scan was initiated 17 minutes after the laser pulse has been delivered, and has run for 62.2minutes.

Many of the peaks observed for early shots were identified as proton generated products. These reactions were undesirable, as in some instances they share emission energies with neutron activation counterparts. For example, 846.8kev is the primary emission of ^{56}Mn (created by ^{56}Fe (n,p) ^{56}Mn) and ^{56}Co from ^{56}Fe (p,n) ^{56}Co. In this case, the secondary emission energies of each product were used to identify and quantify these products. However, the lower probability of decay through the second emission line of ^{56}Mn coupled with lower detector efficiency at the higher gamma energy meant that a significantly higher neutron flux would be required to confirm the presence of the neutron driven ^{56}Mn reaction.
As can be seen in fig. 3, there is a prominent Compton spectrum which has been generated from 511keV photon emissions. It was found that the zinc sample was the primary sample responsible for the Compton spectra. This is most likely generated from the two products of (p,n) reactions from zinc isotopes, ^{64}Ga and ^{66}Ga, which undergo β^+ decay. The Compton spectra edge is an undesirable feature, as it can make the measurement of lower energy emission lines more difficult.

The primary products through neutron activation were identified as ^{115}In (n,n) ^{115m}In, ^{115}In (n,γ) ^{116m}In and ^{56}Fe (n,p) ^{56}Mn.

One of the data sets built from the deconvolution of the energy dependant cross section . The target was a 10μm deuterated polystyrene (CD) foil with a 10mm CD 'catcher' positioned 10mm from the rear of the laser target to intercept generated ion beams and generate more neutrons through D-D fusion events.

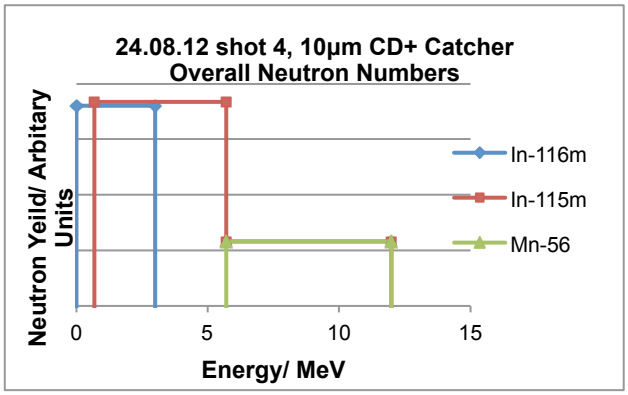

Fig. 4: Absolute numbers of neutrons detected using each activated isotope, against the energy values for their reaction cross sections.

This graph shows the overall number of neutrons inferred from each of the detected neutron activation products from the

sample foils against the neutron energy cross section for that reaction. The ^{56}Fe (n,p) ^{56}Mn reaction is capped at 12MeV as no products of the ^{64}Zn (n,2n) ^{63}Zn with a 12MeV lower energy bound of its cross section are detected. The bracket for the ^{115}In (n,n) ^{115m}In reaction is also reduced to the starting point of the ^{56}Mn cross section. The neutron numbers found from the ^{56}Mn reaction are used to calculate the number of activations of ^{115m}In of this energy, therefore a more accurate number of neutrons below this energy can be determined.

It is more useful to normalise the neutron numbers with respect to energy bin width. The graph of the neutron densities is displayed below in figure 5.

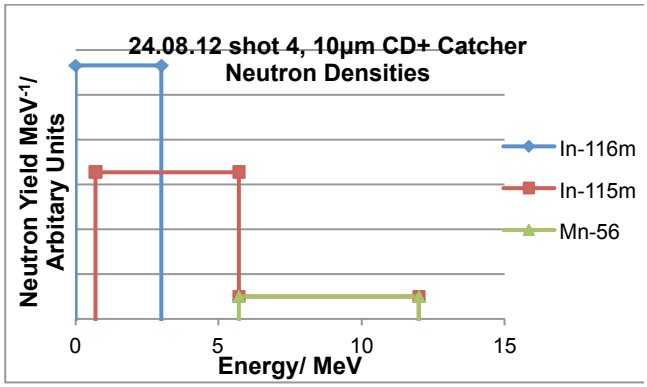

Fig. 5: Neutron spectra with neutron numbers normalised to energy cross section width.

Once the neutron numbers are normalised, it is seen that the highest density of neutrons occur at the lower energies. This suggests that the interaction favours the generation of lower energy neutrons.

Conclusions

It was found that the use of suitably shielded sample foils can be used to determine the neutron spectrum generated on shot. The technique can be used in place or in tandem with more conventional diagnostic tools such as scintillation detectors. As the diagnostic only relies upon the placement of sample foils near to the interaction, and all nuclear detection is carried out away from the interaction chamber, there are no risks to damaging equipment in this extreme environment.
The analysis is also relatively simple, using basic techniques that are easily replicated. Moreover, this technique enables absolute neutron yields to be calculated whilst being able to distinguish between particle types such as protons and gamma emissions, which traditionally cause major issues for traditional detectors that are unable to differentiate between the different emissions.

However, the method does have some limitations. The scanning and analysis of the gamma spectra generated by the activated foils currently takes a considerable time, and the turnover rate of samples is limited by the number of detectors available. There were also limitations on the neutron reactions available within the samples, as it was found that there were fewer activation products created in enough quantity for detection than initially anticipated. This has lead to poor resolution of the resulting neutron energy spectra. This is being improved by better selection of materials for future investigations. Improvements in the shielding of the samples to limit the number of proton activations within the foils and effects from thermal neutrons are also underway.

Acknowledgements

The author would like to thank the experimental group from Queen's University Belfast, Strathclyde and Heinrich Heine universities for providing access to their experiment.

References

1. M. J. Loughlin et al; (2000) 'Neutron Activation Studies on JET', Presented at *21st Symposium on Fusion Technology*, Madrid, 11-15 September 2000
2. Cross section retrieved from Xfor database; http://www-nds.iaea.org/exfor/exfor.htm 10.04.13
3. F. Yang, J. H. Hamilton; (1996) *Modern Atomic and Nuclear Physics*. USA: McGraw-Hill p.571A
4. Berkley National Lab Isotope search tool: http://ie.lbl.gov/toi/radSearch.asp 21.06.13